International Journal of
Molecular Sciences

MDPI

Article

Interrelated Mechanism by Which the Methide Quinone Celastrol, Obtained from the Roots of *Tripterygium wilfordii*, Inhibits Main Protease 3CL^{pro} of COVID-19 and Acts as Superoxide Radical Scavenger

Francesco Caruso *, Manrose Singh, Stuart Belli, Molly Berinato and Miriam Rossi *

Department of Chemistry, Vassar College, Poughkeepsie, NY 12604, USA; manrosesingh@gmail.com (M.S.); Belli@vassar.edu (S.B.); mberinato@vassar.edu (M.B.)
* Correspondence: caruso@vassar.edu (F.C.); rossi@vassar.edu (M.R.)

Received: 17 November 2020; Accepted: 3 December 2020; Published: 4 December 2020

Abstract: We describe the potential anti coronavirus disease 2019 (COVID-19) action of the methide quinone inhibitor, celastrol. The related methide quinone dexamethasone is, so far, among COVID-19 medications perhaps the most effective drug for patients with severe symptoms. We observe a parallel redox biology behavior between the antioxidant action of celastrol when scavenging the superoxide radical, and the adduct formation of celastrol with the main COVID-19 protease. The related molecular mechanism is envisioned using molecular mechanics and dynamics calculations. It proposes a covalent bond between the S(Cys145) amino acid thiolate and the celastrol A ring, assisted by proton transfers by His164 and His41 amino acids, and a π interaction from Met49 to the celastrol B ring. Specifically, celastrol possesses two moieties that are able to independently scavenge the superoxide radical: the carboxylic framework located at ring E, and the methide-quinone ring A. The latter captures the superoxide electron, releasing molecular oxygen, and is the feature of interest that correlates with the mechanism of COVID-19 inhibition. This unusual scavenging of the superoxide radical is described using density functional theory (DFT) methods, and is supported experimentally by cyclic voltammetry and X-ray diffraction.

Keywords: celastrol; methide quinone; COVID-19; thiolate; protease; cyclic voltammetry

1. Introduction

Human use of plants as sources of medicinal benefit predates written history, and there is a growing interest in traditional plant-based medicines. Celastrol is a methide quinone triterpene isolated from the roots of *Tripterygium wilfordii*, or "God of Thunder" vine. It has been used in traditional Chinese medicine for hundreds of years [1] to treat chronic inflammations, autoimmune conditions, neurodegenerative diseases, and cancer-related symptoms [2–4]. Toxicity concerns may limit celastrol administration as a drug. In a specific toxicity test, different doses of celastrol were orally administered to mice [5] and showed no significant changes. However, side effects of celastrol administration have been reported, for instance, cardiotoxicity upon chronic treatment [6], and infertility [7]. To overcome celastrol solubility and pharmacokinetic issues, several methodologies have been tested, such as exosomes [8], lipid nanospheres [9], nanoencapsulation [10], liposomes [11,12], polymeric micelles [13,14], sugar-silica nanoparticles [15], and a self-microemulsifying drug delivery system [16]. For instance, celastrol-loaded mesoporous silica nanoparticles that are sugar-decorated have shown increased specific anticancer activity with no induced toxicity in HeLa and A549 cells [15]. Celastrol is also implicated in the

NF-κB pathway [17] by interacting with the IKK kinases in a dose-dependent manner. Thus, celastrol likely contributes to its anti-inflammatory and anti-tumor activities by inhibiting NF-κB activation possibly through targeting Cys-179 in IKK-β [18]. Indeed, celastrol interactions with thiol groups have already been described in the literature: (1) celastrol can react with protein thiols in human cervical HeLa cells in a unique covalent and reversible manner [19]. (2) Its quinone methide structure can react specifically with the thiol groups of cysteine residues, forming covalent protein adducts [20]. (3) It shows thiol-related effects on the human monocytic leukemia cell line U937 proliferation [21]. (4) The cytotoxic effect of ionizing radiation in vitro is enhanced with celastrol administration, and its quinone methide moiety is essential for this radiosensitization. Celastrol induced the thiol reactivity and inhibited the activities of antioxidant molecules, such as thioredoxin reductase and glutathione [22]. In addition, reactive oxygen species production by ionizing radiation was augmented. (5) Celastrol promotes proteotoxic stress, supported by the induction of heat-shock proteins, HSP72, through a thiol-dependent mechanism; these findings imply that celastrol targets proteostasis by disrupting sulfyhydryl homeostasis in human glioblastoma cells [23]. (6) In addition, it was seen that celastrol reduced lipopolysaccharides (LPS)-induced expression of inflammatory cytokines, such as tumor necrosis factor (TNF)-α, interleukin (IL)-6, IL-12, and IL-1β. These inhibitory effects of celastrol on LPS were reversed by thiol donors (N-acetyl-L-cysteine and dithiothreitol), suggesting that the thiol reactivity of celastrol contributes to its inhibitory effects on macrophages. These results provide a novel mechanism of action by which celastrol contributes to the anti-inflammatory activity of *T. wilfordii* [24]. This is of interest, since inflammatory symptoms are present in coronavirus disease 2019 (COVID-19) patients, including an unusual multisystem inflammatory syndrome in children (MIS-C). (7) Celastrol's biological effects, including inhibition of glucocorticoid receptor activity, can be blocked by the addition of excess free thiol, suggesting a chemical mechanism whereby this natural product could modify key reactive thiols [25].

The interaction between cysteine and quinones has been noted [26] and includes a recent description of the quinone embelin establishing an important covalent bond with Cys145 of the main COVID-19 protease $3CL^{pro}$ to explain the inhibitory mechanism [27]. Since the methide quinone celastrol shows inhibition towards SARS-CoV $3CL^{pro}$ [28], such an association between celastrol and the active site cysteine in the COVID-19 protease is supported. Moreover, celastrol antiviral activity is described for infectious bronchitis virus [29], influenza A [30], hepatitis C [31], dengue [32], and HIV [33].

Indeed, our described quinone embelin inhibition mechanism on $3CL^{pro}$ implicates Cys145 assisted through H-bonds from nearby amino acids, and strongly resembles the mechanism of embelin antioxidant activity toward the superoxide radical [34,35]. Both of these two chemical reactions underscore quinone electron affinity. The superoxide transfers its unpaired electron to the quinone embelin through a π–π interaction [34,35], while in the main protease the Cys145 thiolate is also π attracted by the embelin quinone centroid, as seen in docking results. This driving force contributes to the formation of a covalent bond between S(thiolate) and an embelin positively charged carbonyl moiety [27]. Specifically, the Cys145-His41 diad, conserved in all versions of SARS viruses, provides the perfect arrangement for cleavage of the (Cys145) S-H bond assisted by the N-imidazole(His41) acceptor in the embelin case. Finally, among the most effective repurposed drugs against COVID-19 is the corticosteroid dexamethasone [36], which is a methide quinone (as celastrol), and which acts in a similar way as embelin [27]. Its mechanism of action on the main protease $3CL^{pro}$ is also similar to methyl prednisolone [37], another corticosteroid methide quinone used against COVID-19 [38]. Therefore, the association of celastrol anti-SARS inhibition activity, IC_{50} of 10.3 μM [28], with a similar related mechanism seems apparent. Here, we describe the mechanism of celastrol, Scheme 1, at the active site of the main COVID-19 protease, $3CL^{pro}$, using crystal structure, electrovoltaic antioxidant measurements, docking, and density functional theory (DFT) methods.

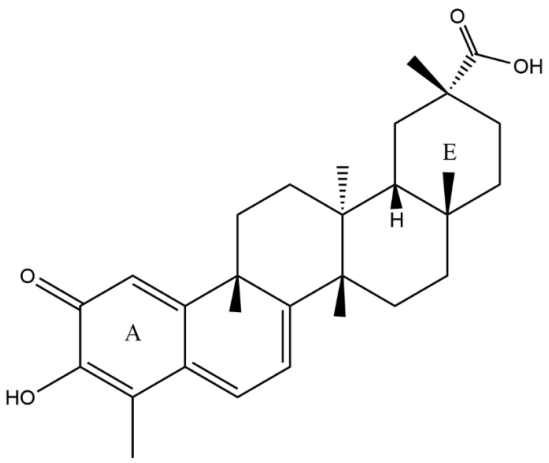

Scheme 1. Celastrol.

2. Results and Discussion

2.1. X-ray Diffraction

Beautiful yellow crystals of celastrol were obtained after solvent evaporation in chloroform solution. These crystals were isostructural to an acetonitrile solvated crystal structure of celastrol [39,40]. The asymmetric unit contains two celastrol molecules along with a solvent chloroform molecule. The two molecules form a striking elliptical dimeric structure through two pairs of strong hydrogen bonds at either end of the celastrol molecule. The solvent molecule lies outside of this dimer (see Figure 1). The H-bond values at one end of the dimer are O1-H1···O104 2.842(6) Å and angle 145.8°, and O103-H103···O2 2.607(6) Å and angle 177°, while at the other end of the dimer they are O3-H3···O102 2.573(5) Å and angle 169°, and O101-H101···O4 2.948(5) Å and angle 151°. Each of the two molecules also shows an intramolecular hydrogen bond between the carbonyl oxygen and the adjacent hydroxyl group: O1-H1···O2 2.741(7) Å and angle 113°, and O101-H101···O102 2.707(6) Å and angle 115°. The two molecules do not differ very much, and a superposition of them shows little variation. The three saturated rings are in a chair conformation. Ring B, adjacent to the planar methide quinone ring, is almost coplanar in an envelope conformation with the substituted C6 atom being 0.25 Å out of the plane as seen in Figure 2.

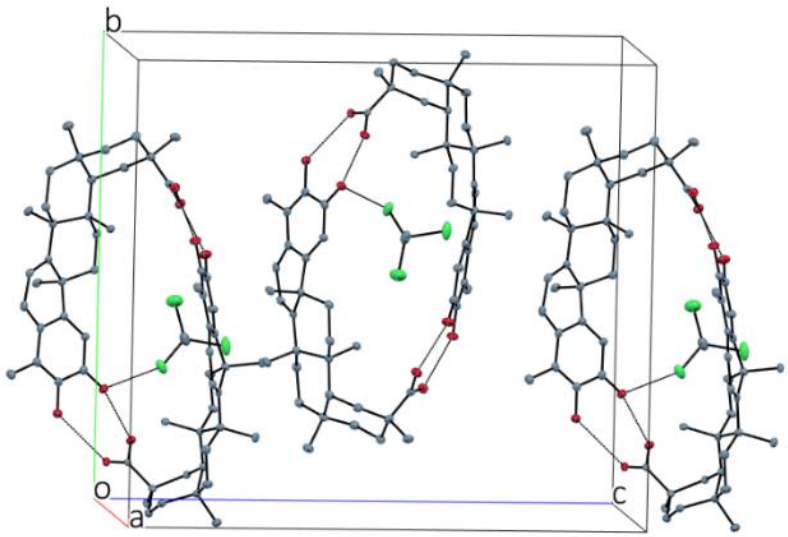

Figure 1. Three-dimensional packing of the dimeric celastrol molecules. The solvent chloroform molecule is not in the hole. H atoms not shown.

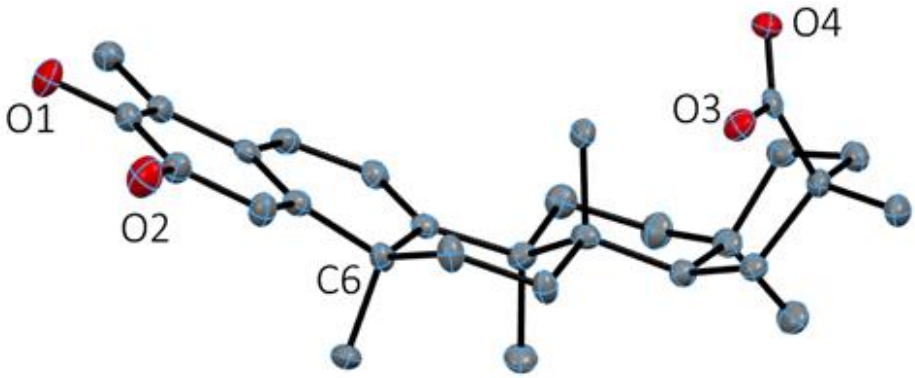

Figure 2. Celastrol molecule showing the conformation of the individual rings: planar for the methide quinone ring A on the left; envelope with C6 out of plane for adjacent ring B; remaining three rings are in chair conformation. H atoms are not shown for clarity.

The chloroform solvent provides for additional intermolecular interactions in the crystal: a hydrogen bond C1S-H1S···O4 (donor-acceptor 3.234(9) Å) and C-H-O bond angle 141° along with a halogen bond between Cl2 and the carbonyl O102 of celastrol at a distance of 3.088 Å, shorter than the sum of van der Waals radii, and with the C-Cl-O angle of 155°, Figure 3. Table 1 shows crystal data.

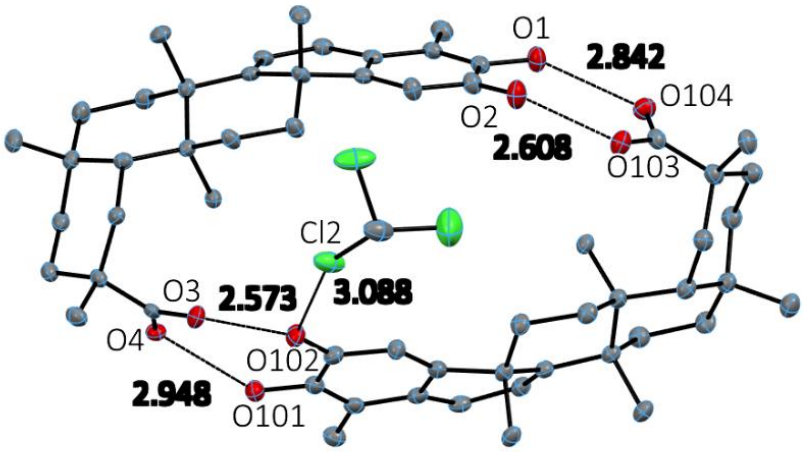

Figure 3. Asymmetric unit dimeric structure with chloroform solvent showing H-bond and halogen bond distances. H atoms not shown for clarity.

2.2. Electrochemistry

The antioxidant capability of celastrol towards the superoxide radical was studied using a variation of classic cyclovoltammetry with a rotating ring disk electrode (RRDE) method recently developed by our lab [41]. The superoxide radical is generated in situ in a voltaic cell using anhydrous dimethyl sulfoxide (DMSO) as solvent, through bubbling of a controlled amount of oxygen. The superoxide radical is obtained at enough negative potential so that O_2 captures an electron from the working electrode

$$O_2 + e^- \rightarrow O_2^{-\bullet} \quad (1)$$

The configuration of the voltaic cell includes, besides the working rotating disk electrode, a reference electrode and a ring electrode around the disk. The ring potential is chosen positive enough for oxidation of the superoxide so that the reaction opposite to **(1)** is performed. The progressive amounts of antioxidant added (celastrol) to the voltaic cell allow us to measure the consumed superoxide (at the ring electrode) more precisely than when using only one working electrode in classical cyclovoltammetry [41].

Table 1. Crystal data for celastrol.

Chemical formula	$2(C_{29}H_{38}O_4)$ ($CHCl_3$ *solvent*)	
Formula weight	450.6 g/mol	
Temperature	125(2) K	
Wavelength	1.54178 Å	
Crystal system	orthorhombic	
Space group	P 2_1 2_1 2_1	
Unit cell dimensions	a = 12.3174(19) Å	
	b = 19.764(4) Å	α = 90°
	c = 22.017(3) Å	β = 90°
Volume	5359.8(17) $Å^3$	γ = 90°
Z	8	
Density (calculated)	1.265 g/cm^3	
Absorption coefficient	1.978 mm^{-1}	
F(000)	2184	
Theta range for data collection	3.00 to 68.23°	
Index ranges	$-14 \leq h \leq 14$, $-23 \leq k \leq 23$, $-25 \leq l \leq 26$	
Reflections collected	60772	
Independent reflections	9745 [R(int) = 0.1955]	
Coverage of independent reflections	99.7%	
Absorption correction	Multi-scan	
Refinement method	Full-matrix least-squares on F^2	
Refinement program	SHELXL-2014/6 (Sheldrick, 2014)	
Function minimized	$\Sigma\, w(F_o^2 - F_c^2)^2$	
Data/restraints/parameters	9745/0/649	
Goodness-of-fit on F^2	1.059	
Final R indices	7424 data; $I > 2\sigma(I)$	R1 = 0.0641, wR2 = 0.1465
	all data	R1 = 0.0896, wR2 = 0.1653
Weighting scheme	$w = 1/[\sigma^2(F_o^2)]$ where $P = (F_o^2 + 2F_c^2)/3$	
Extinction coefficient	0.0018(3)	
Largest diff. peak and hole	0.421 and −0.484 $eÅ^{-3}$	
R.M.S. deviation from mean	0.101 $eÅ^{-3}$	

Celastrol is a methide quinone having two hydroxyl groups, Scheme 1, and these may be involved in sequestering superoxide, as clarified through DFT calculation. From the RRDE graph, Figure 4, it is seen that progressive amounts of celastrol decrease but cannot deplete the superoxide content in the voltaic cell. The signal detected at the ring electrode is located at the upper part of the graph, and shows that at the maximum celastrol concentration, 9.0×10^{-5} M, there is still superoxide in the voltaic cell.

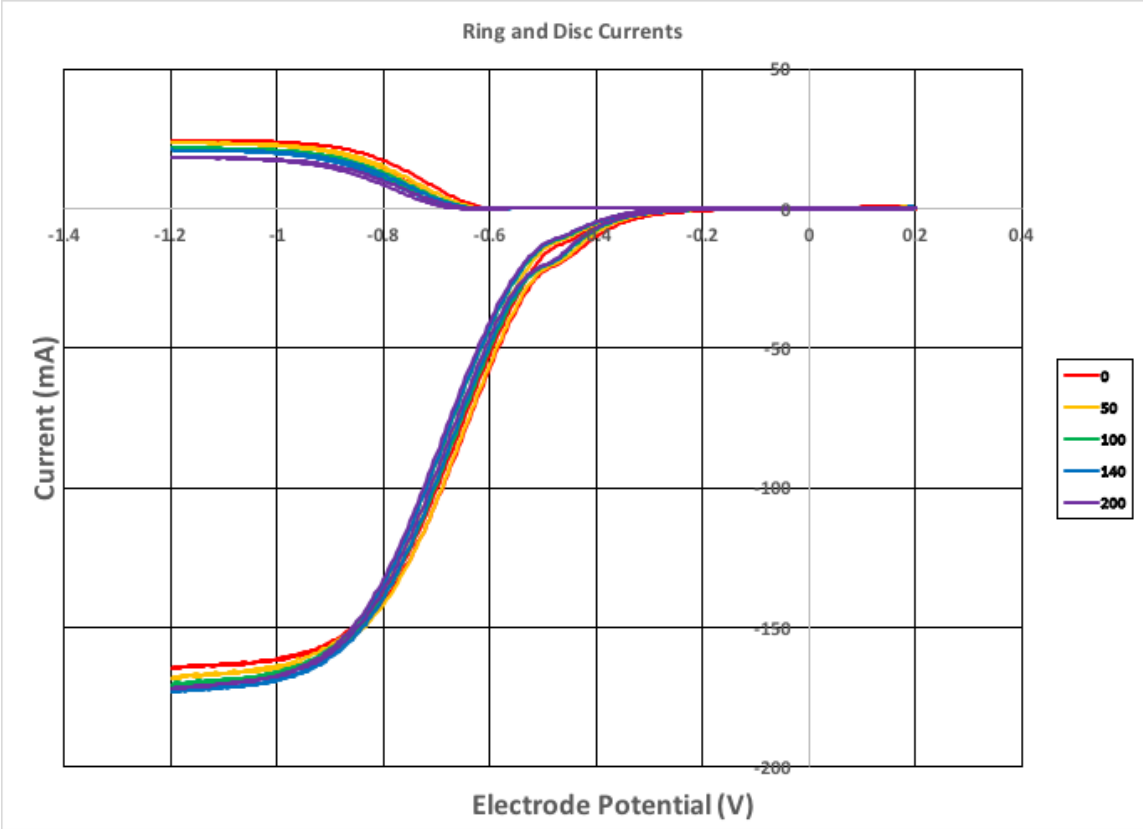

Figure 4. Rotating ring disk electrode (RRDE) voltammograms showing only 5 lines out of 15 for clarity, indicating the volume of aliquots added. The complete set of 15 data is shown in Figure 5.

The collection efficiency is the ratio between current at the ring and the disk for any studied solution, and the slope is the indicator of antioxidant capability. Therefore, celastrol slope, -5.9×10^4, compares well with emodin -6.0×10^4 [42]; it is more active than embelin, -2.8×10^4 [34], and weaker than quercetin, -15.4×10^4 [34] (all measured following the same experimental protocol). Since celastrol is a better scavenger of superoxide than embelin, which has been identified as an inhibitor of the main COVID-19 protease [28], we consider if celastrol might be a better inhibitor.

2.3. DFT Antioxidant Properties

Polyphenol action for scavenging radicals is generally based on the capability of radical induced cleavage of a hydroxyl H atom bound to the aromatic ring (option ***a***). The original radical, after binding the H atom, becomes electron paired, while the former polyphenol becomes a newly formed, more stable radical since the unpaired electron relocates within the aromatic ring framework and is less likely to react with other molecules. However, a second possibility of scavenging (option ***b***) is feasible when the ring system captures only the electron directly from the original radical, leaving the polyphenol aromatic hydroxyls unaffected. Very probably, option (***b***) is favored when polyphenol hydroxyls are inaccessible, for instance, due to strong H-bonds. Interestingly, option (***b***) is better suited when a scavenger contains a quinone ring rather than an aromatic system. Our lab has studied the quinones embelin and emodin [34,42], two natural products, and we found that they prefer option (***b***).

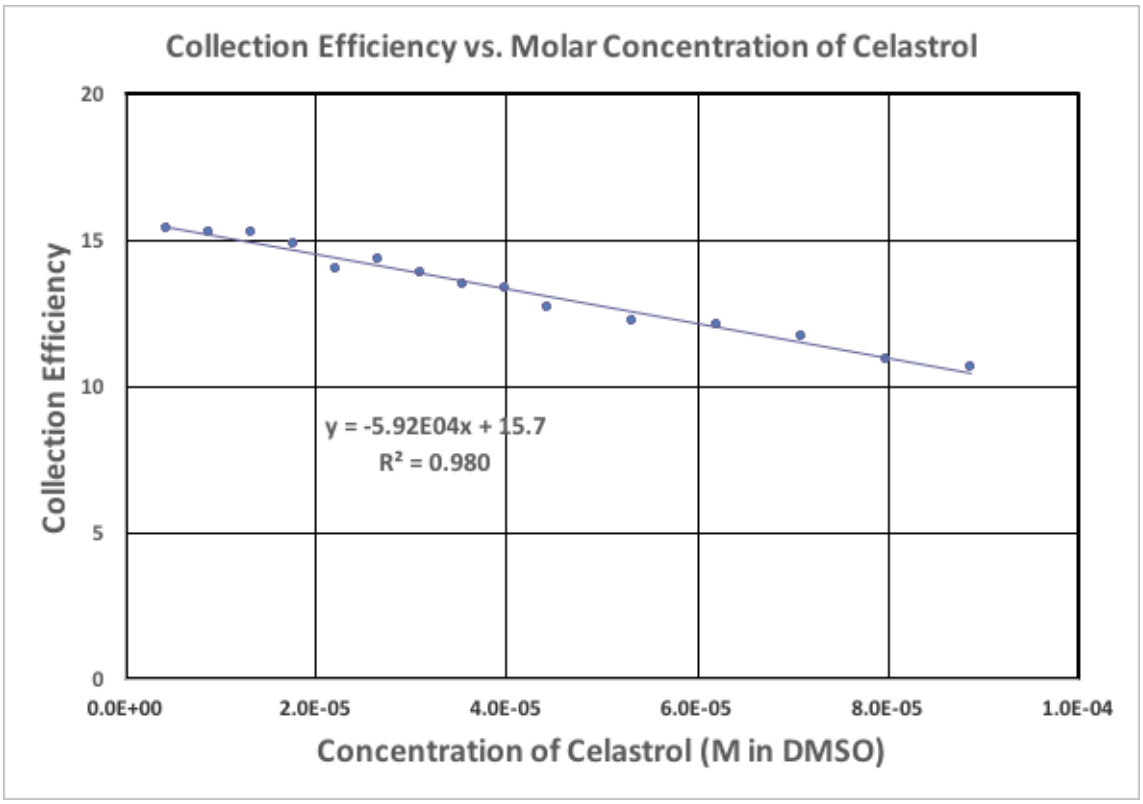

Figure 5. Collection efficiency of celastrol.

Figures 6 and 7 show the approach of superoxide to a hydroxyl belonging to a simplified celastrol model, used to decrease calculation time. Initial coordinates of one celastrol molecule were obtained from our X-ray diffraction study. After DFT geometry optimization, the transfer of only one electron from the superoxide radical to the methide quinone ring is seen, which illustrates option (***b***). Figures 8 and 9 show the equivalent approach through a π-π interaction, with equal results. Results of more extensive calculations are shown in Figures 10 and 11, where the complete molecule of celastrol shows additional reactivity. Thus, after van der Waals π-π interaction by a hydronium H_3O^+ cation to the O=C-COH moiety, a proton is captured by the O(carbonyl), with formation of a molecule of water. After elimination of water and O_2 from Figure 10 structure, the resulting neutral semiquinone can further react with an additional superoxide, see Figure 11, leading to option (***a***) mode of radical scavenging by polyphenols described earlier. Formation of H_2O_2 would follow when interacting with an additional proton. The whole process is able to sequester more than one superoxide radical, the first σ or π reacted radical is followed by H_3O^+ in Figure 5, and an additional superoxide shown in Figure 6. The outcome of this process is therefore defined by the availability of superoxide and protons, and illustrated in the RRDE section. That is, superoxide radical anions are abundantly provided by the voltaic potential, whereas not completely anhydrous DMSO solvent and/or air environmental humidity can influence the RRDE outcome.

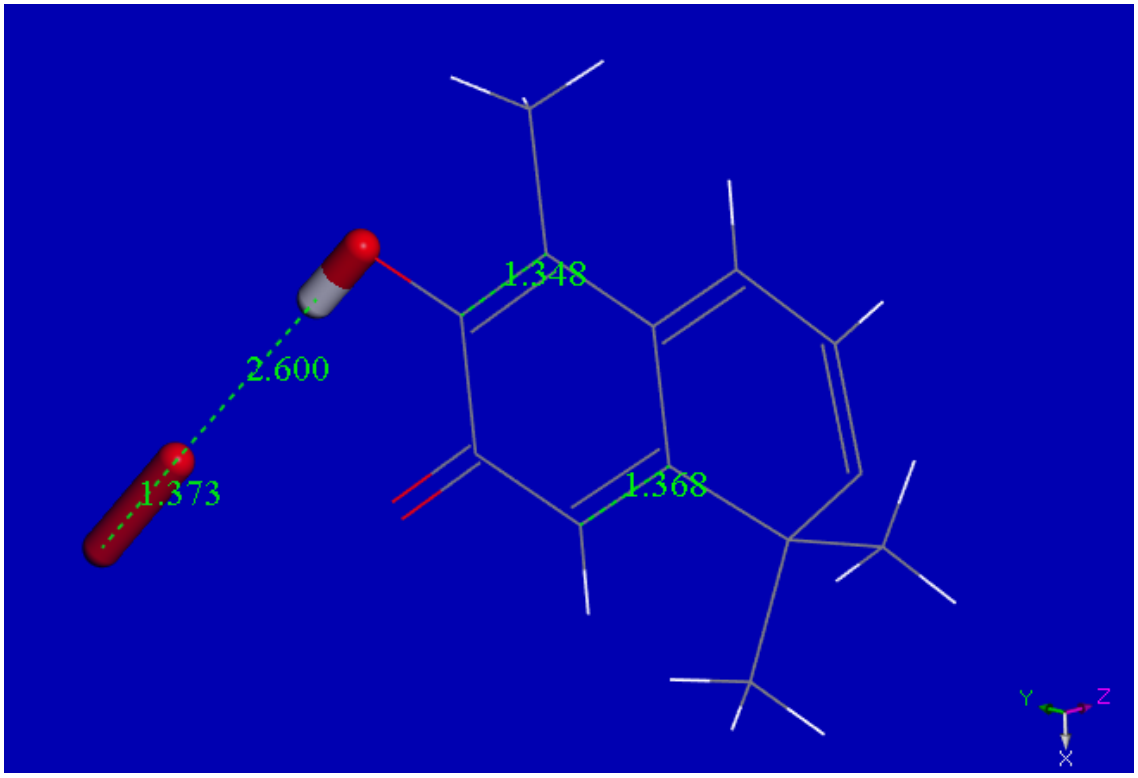

Figure 6. Superoxide σ approached by model celastrol. The celastrol hydroxyl is separated from superoxide by van der Waals distance, 2.60 Å. This is the initial state.

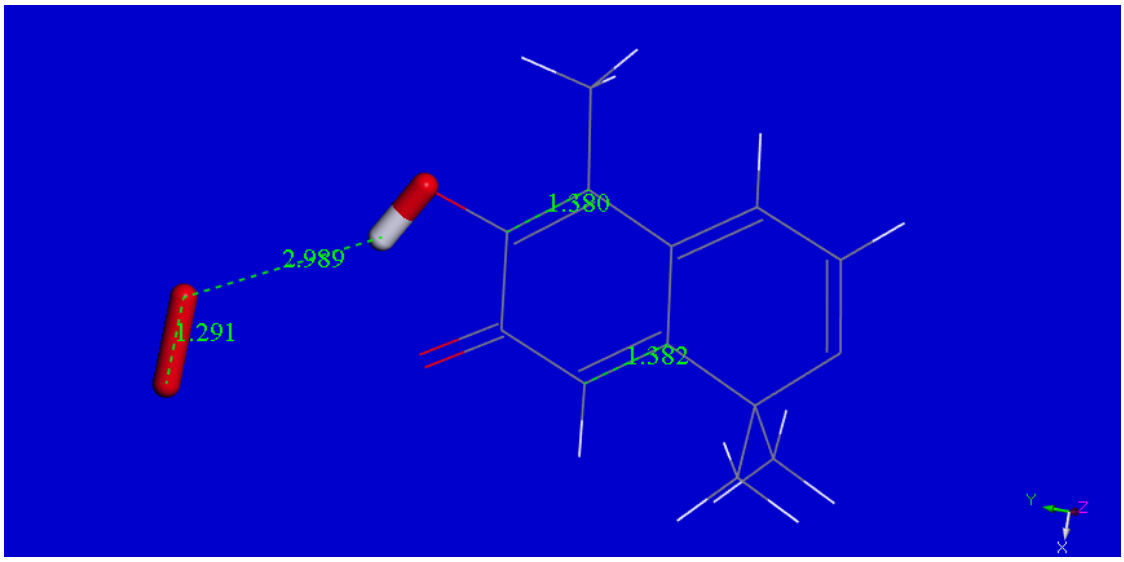

Figure 7. Superoxide σ approached by model celastrol, final state obtained after geometry optimization. The capture of the superoxide electron causes the double C-C bond in the ring to become lengthened (1.380 Å and 1.382 Å); the O_2 molecule separates from celastrol (2.989 Å), and the former superoxide has shortened its O-O bond, 1.291Å, compared with the initial state distance, 1.373 Å. This process does not involve H(hydroxyl) cleavage, as commonly happens for scavenging by polyphenols.

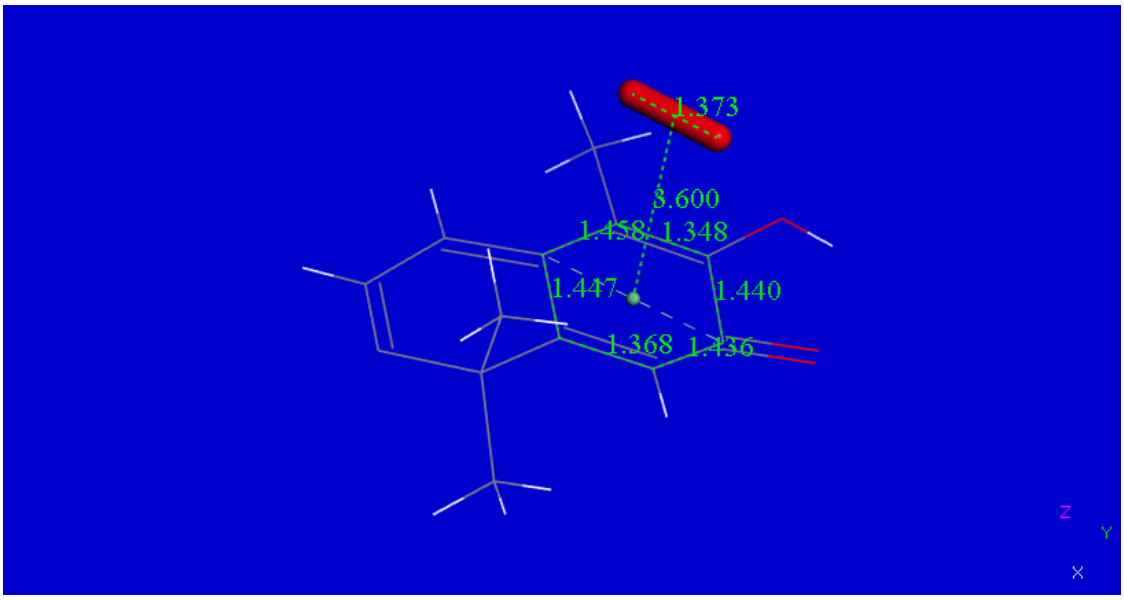

Figure 8. Superoxide π-π approached by model celastrol. Initial state.

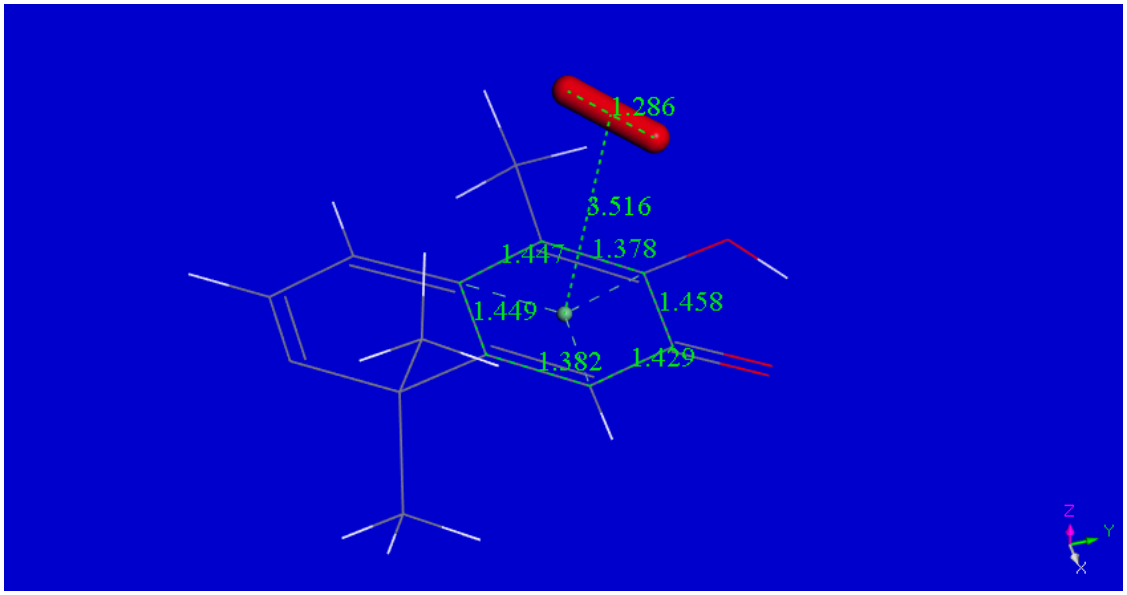

Figure 9. Superoxide π-π approached by model celastrol, final state, obtained after density functional theory (DFT) geometry optimization. Comparing with Figure 8, there is lengthening of the ring C-C double bonds, 1.382 Å and 1.378 Å, and shortening of O-O bond, 1.286, due to O_2 formation.

Additional examination of the celastrol antioxidant action through its ring E carboxylic moiety is now described. Geometry optimization of the arrangement containing the initial van der Waals-separated moieties [O(superoxide)—H(carboxylic moiety)] is shown in Figure 12. When the van der Waals-separated probable product [O_2H—Celastrol-carboxylate] was geometry-optimized the same structure seen in Figure 12 was obtained. Thus, the DFT analysis shows the formation of a stable complex between superoxide and celastrol when interacting through its carboxylic acid moiety. Furthermore, the LUMO shown in Figure 12 suggests that the carboxylic-superoxide complex does not preclude further reactivity at ring A. Therefore, celastrol demonstrates strong antioxidant activity (Figures 7 and 9–11) through the combination of superoxide scavenging and incorporation of protons (ring A) as well as its capability to stabilize an additional superoxide molecule at the other end of the molecule, ring E, Figure 12.

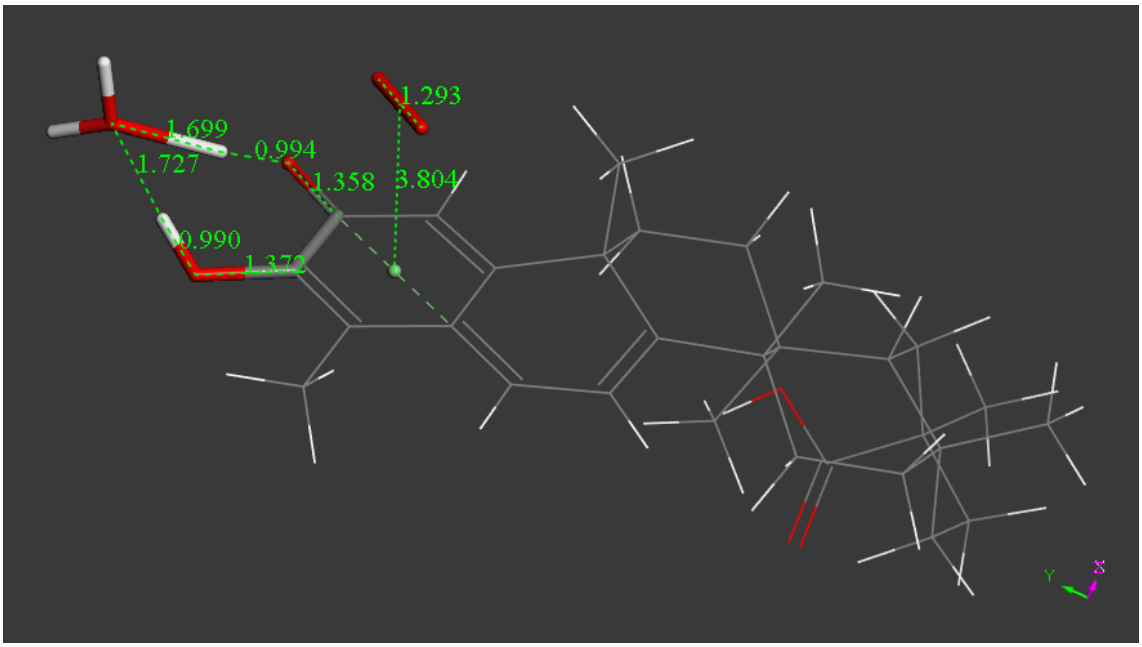

Figure 10. Geometry optimization of the complete celastrol molecule. When superoxide is π stacked on the celastrol quinoid ring, an electron is captured by the latter. Later, an H_3O^+ approach to the ring carbonyl induces proton capture, d[(C=O)-H] = 0.994 Å, plus water formation. Total charge of this semiquinone species is zero due to the charged negative superoxide (−1) plus the H_3O^+ charge.

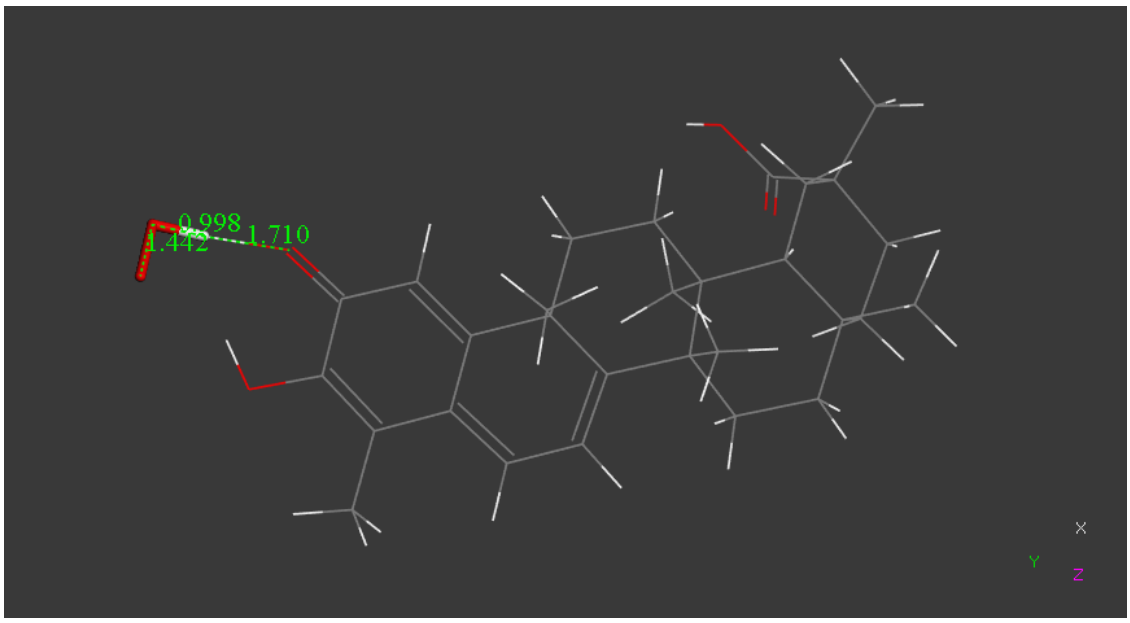

Figure 11. From Figure 10, the water and the O_2 molecules were eliminated and the remaining species contains a catechol moiety. Hence, a potential approach of another superoxide is able to sequester a H atom, d(O_2-H) = 0.998 Å, forming the O_2H species. This is the classical manner of scavenging radicals by polyphenols, (option ***a***). Total charge is −1, due to O_2H. Interestingly, the O_2H^- species in turn can capture a proton to form H_2O_2.

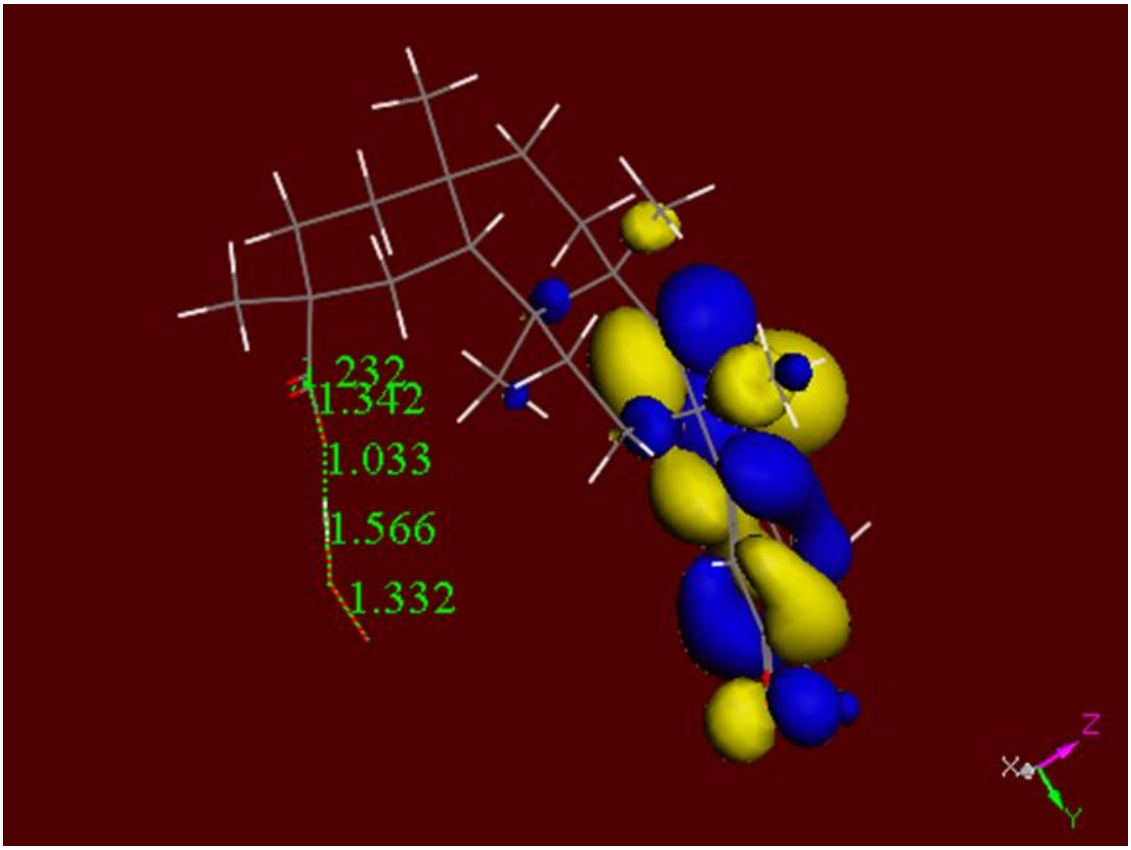

Figure 12. LUMO for the complex celastrol-carboxylic-moiety-superoxide, total charge −1. LUMO indicates further reactivity in the methide quinone area of this complex.

2.4. Docking the Protease COVID-19 3CL^{pro}

The SARS 3CL^{pro} protease active site was obtained after downloading coordinates from the PDB database, PDB ID: 6LU7 [43]. The published protein included the inhibitor N3 and was treated with the Discovery Studio "prepare protein" protocol, which provides assignment of CHARMm force field and addition of H atoms. The inhibitor was removed and the binding site was chosen after selecting Cys145 and His41 amino acids, for a sphere of radius 14 Å. Results of docking celastrol (15 poses) were analyzed focusing attention on interactions between S(Cys145) and the methide quinone centroid, which were found in closely related poses 5, 13, and 14. Pose 5 has CDOCKER interaction energy of −41.7 kcal/mol and was selected for further study. Figure 13 displays essential amino acids useful for description of the mechanism. Pose 5 was also treated with Discovery Studio standard dynamic cascade protocol, Figure 14, and results show a marked increase in interactions between celastrol and the active site. Thus, H(His41) H-bond to celastrol carbonyl of 3.184 Å (docking) gets shorter after dynamics (2.181 Å); S(Cys145) directed to the quinoid carbonyl, 4.612 Å (docking), becomes slightly closer after dynamics, 4.559 Å. The dynamic cascade shows O(His164) H bond to H-S(Cys145) of 2.138 Å, suggesting H capture and thiolate formation, for further attack on the celastrol carbonyl by the latter. Thus, capture of H(His41) by the celastrol carbonyl, and O(His164) capture of H-S(Cys145) generating S(Cys145) thiolate, are shown in Figure 15, having the S(thiolate) pointing to the celastrol C(carbonyl), 3.347 Å. In addition, further stabilization of the celastrol-protease complex is provided by Met49, which was initially distant from celastrol in docking pose 5, but after dynamic cascade gets closer to the ring B centroid of celastrol, 4.480 Å, establishing a π interaction, in agreement with ring B capability to interact with nucleophilic S atoms [20]. The 2D interaction display for celastrol after dynamic cascade is shown in Figure 16, while that for Cys145 showing H-bond to O(His164) is depicted in Figure 17.

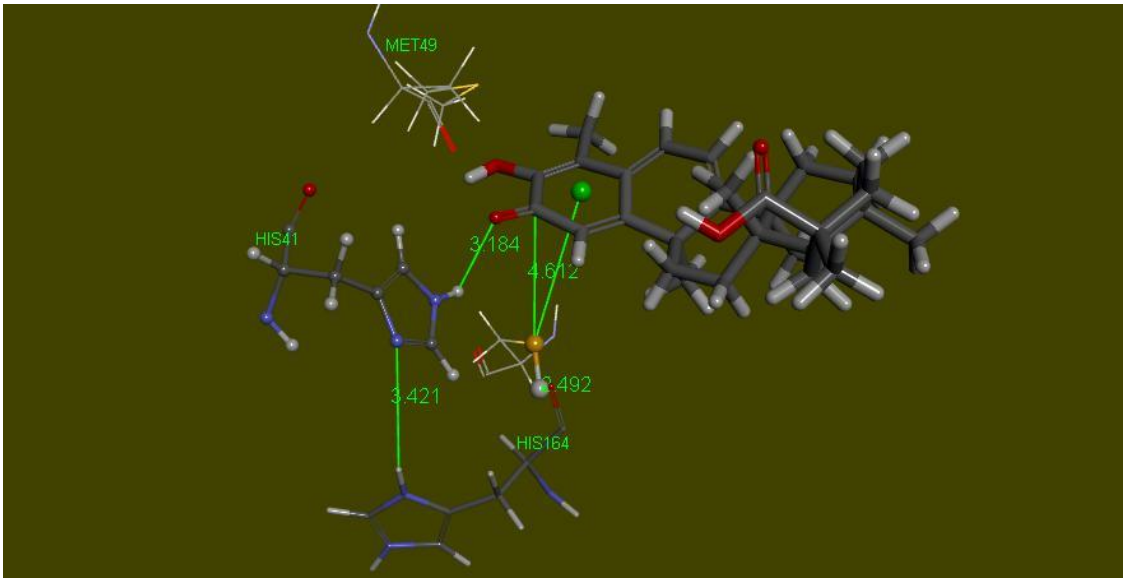

Figure 13. Docking pose 5 displays the essential amino acids, Cys145 (line style, not labeled for clarity), His41 (ball style), Met49 (line style), and His164 (stick style). S(Cys145) points to the quinoid ring centroid, 4.989 Å (value not shown for clarity), and the quinoid carbonyl, 4.612 Å. Met149 is rather detached from ring B centroid.

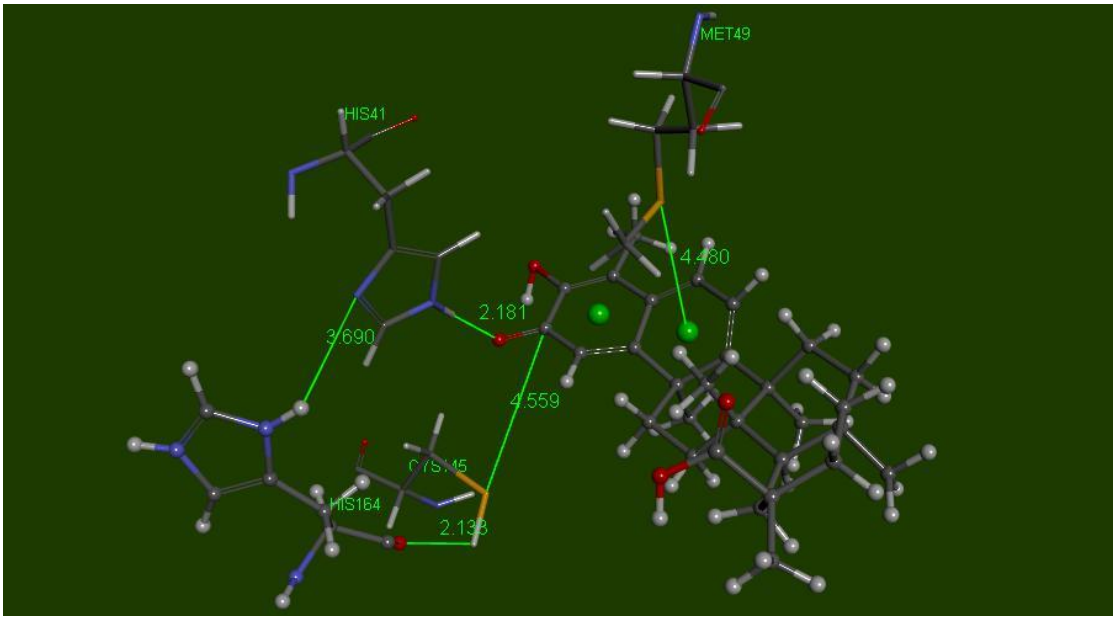

Figure 14. Result of dynamic cascade of docking pose 5 displays His41 closer to the methide quinone carbonyl than in the docking results, d(H-NImidazole) = 2.181 Å, and 3.184 Å, respectively, inducing H capture by the carbonyl. Additionally, O(His164) is closer to H(Cys145), 2.133 Å, compared with the docked structure of 2.492 Å, suggesting H(Cys145) detachment and formation of S(Cys145) thiolate. An evolution of this structural arrangement is shown in Figure 15.

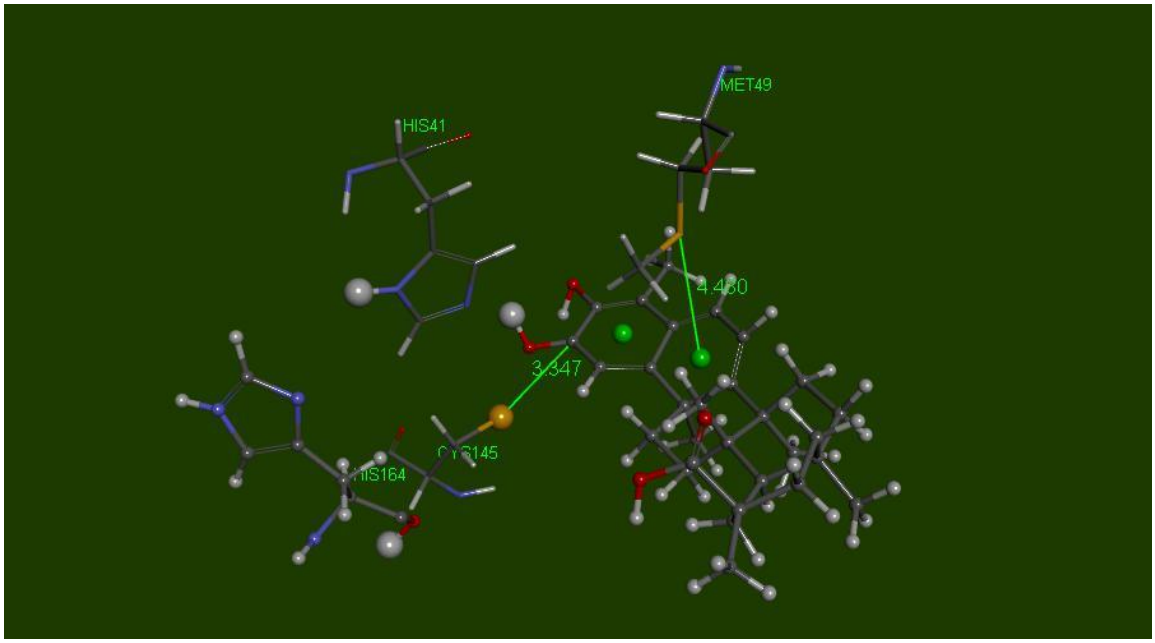

Figure 15. This shows O=C(Celastrol) capture of H(imidazole-His41) forming a positively charged HOC(celastrol) moiety, and the Cys145 S-H cleavage due to proton capture by O(His164) forming HO(His164). After rotating the Cys145 torsion angle C-C-C-S, the S(thiolate) gets closer to the former celastrol C(carbonyl), 3.347 Å, to form a S-C covalent bond.

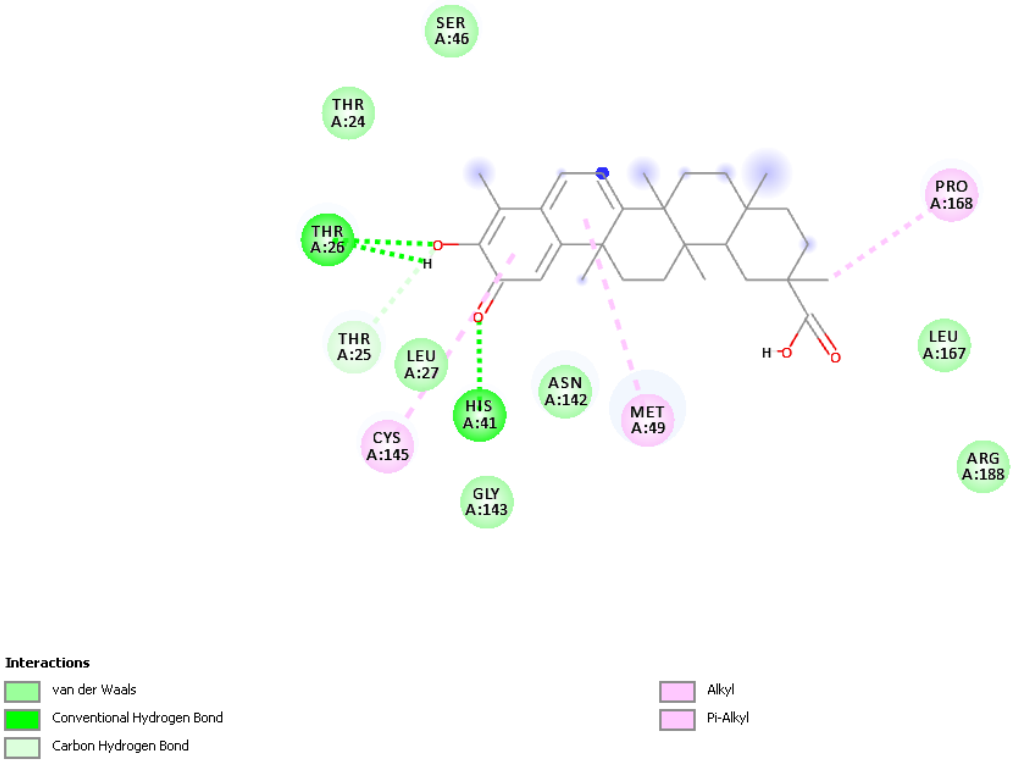

Figure 16. 2D display of Celastrol pose 5 after dynamic cascade.

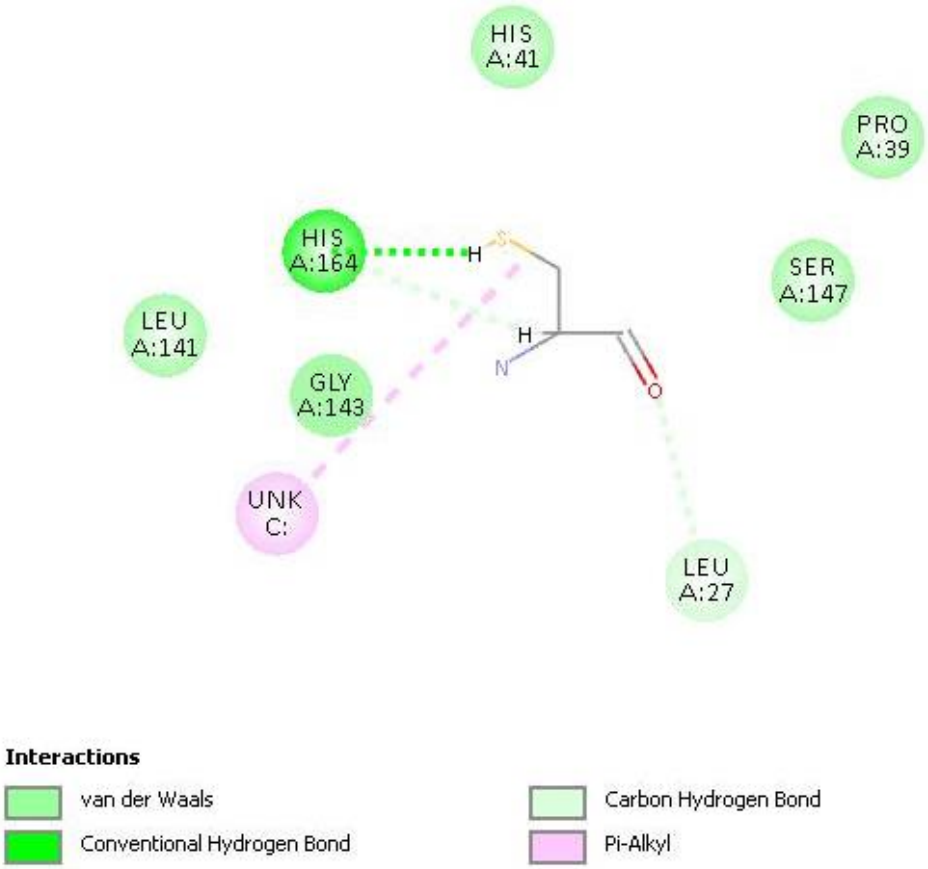

Figure 17. 2D interactions after dynamic cascade of Cys145 shows H-bond to O(His164), suggesting SH cleavage.

In conclusion, celastrol is a methide quinone compound obtained from the roots of *Tripterygium wilfordii* and used in traditional Chinese medicine. Celastrol also shows a large variety of interesting biological properties, including inhibition of COVID-19. In this study, we describe celastrol interaction with the active site of the COVID-19 virus main protease. We also include a crystal structure analysis of celastrol and disclose its uncommon antioxidant capability when scavenging the superoxide radical, by using DFT methods. Thus, there are two chemical moieties in celastrol able to scavenge the superoxide radical: the carboxylic framework of ring E, and more importantly, the methide quinone located at ring A. The latter captures the superoxide electron, releasing molecular oxygen. This unusual scavenging of the superoxide radical is supported experimentally by cyclic voltammetry and X-ray diffraction. We observe a correlation between antioxidant property and protease inhibition, through a specific interaction of celastrol with the Cys145 amino acid, assisted by proton transfer at the active site. The final complex formed between celastrol and Cys145 thiolate is further stabilized by a π-bonding between Met49 and the B ring of celastrol.

Therefore, our proposed mechanism for celastrol inhibition, based on molecular dynamics, is shown in Scheme 2 and consists of (1) proton donation to celastrol O(carbonyl) by HN(His41) and (2) cleavage of S-H bond in Cys145 by His164. These first two steps determine formation of intermediate (3). Subsequently, (4) attack of S(thiolate)-Cys145 to celastrol former O(carbonyl) and (5) S(Met49) π bonding to the ring B centroid define the final product that inhibits the protease.

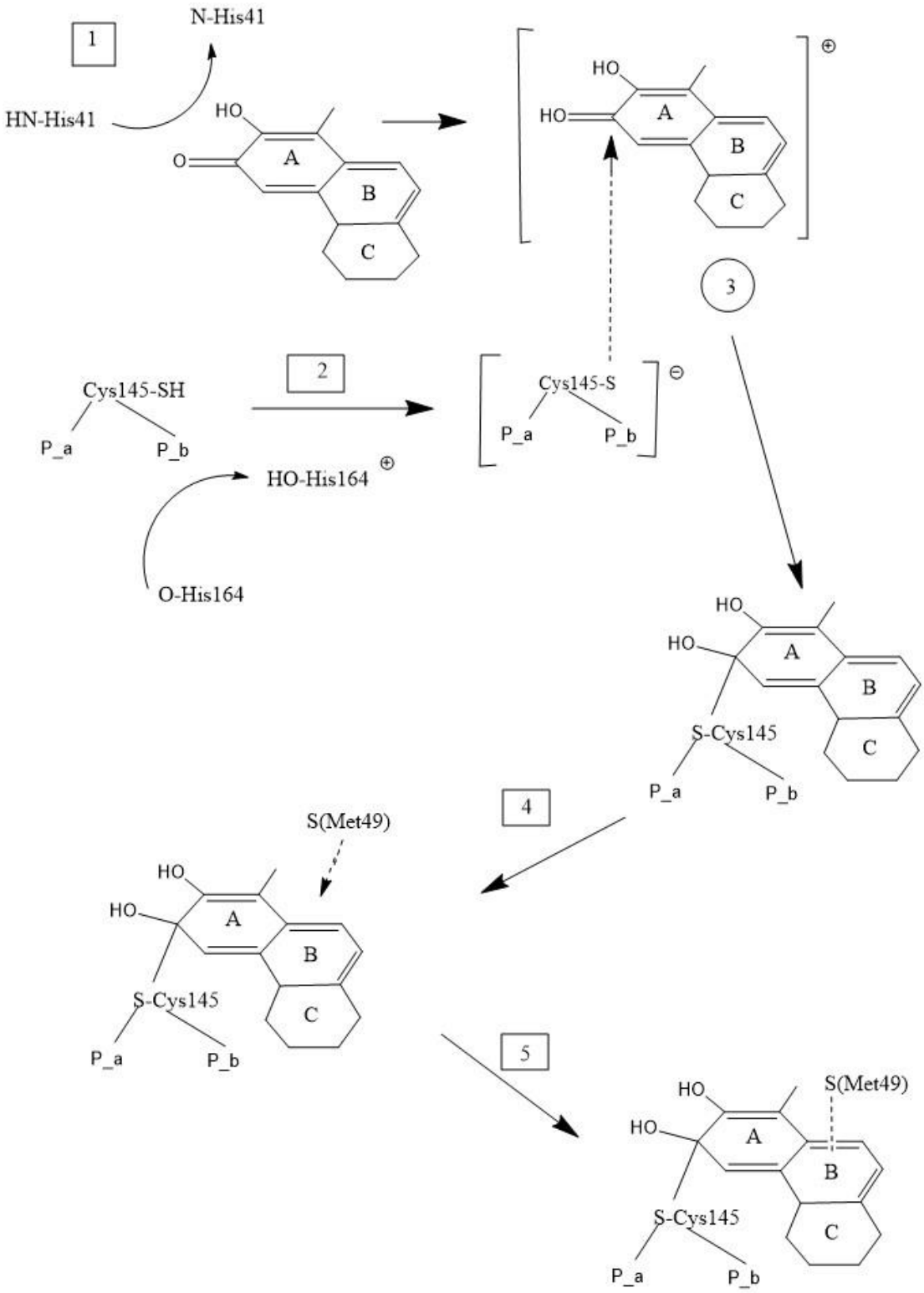

Scheme 2. Mechanism of main COVID-19 protease inhibition by celastrol. P_a and P_b represent the peptide chain associated with Cys145. Only three rings of celastrol are shown for clarity. (1) HN(His41) donates a proton to celastrol carbonyl; (2) O(His146) captures HS(Cys145), generating the S(Cys145) thiolate. Joining products of steps (1) and (2) generates species (3) that stabilizes the S-C(carbonyl) covalent bond; (4) Met49 points to celastrol ring B centroid; (5) Met49 forms a S-π interaction with ring B centroid, so that celastrol finally establishes a double interaction with Cys145 and Met49, of the COVID-19 protease.

Finally, this study of celastrol was stimulated by its already described anti-SARS-2 biological activity [28], and how its methide-quinone structural features compare with the embelin mechanism on COVID-19 main protease inhibition [27]. Celastrol-COVID-19 investigation is also encouraged because of promising in vivo results from celastrol on a variety of lung related disorders [44]. Our results allow us to correlate the antioxidant property of celastrol, when scavenging the superoxide radical, with its inhibitory profile on the main protease COVID-19 active site. We also describe the inhibitory detailed mechanism of celastrol, based on docking and dynamics molecular mechanics.

3. Materials and Methods

3.1. Chemicals

Celastrol (Cayman, Ann Arbor, MI, USA). Dimethyl sulfoxide (DMSO, anhydrous, ≥99.9%), tert-butyl ammonium bromide (TBMA), [(2,2-dimethyl-6,6,7,7,8,8,8-heptafluoro-3,5-octanedionato)silver(I)], (Sigma-Aldrich, St. Louis, MO, USA)

3.2. Equipment

Hydrodynamic voltammetry at a rotating ring-disk electrode (RRDE) was carried out using the Pine Research (Pine Research, Durham, NC, USA) WaveDriver 20 bipotentiostat with the Modulated Speed Electrode Rotator. The working electrode is the AFE6R2 gold disk and gold ring rotator tip (Pine Research, Durham, NC, USA), combined with a coiled platinum wire counter electrode and a reference electrode consisting of an AgCl coated silver wire immersed in 0.1 M TBAB in dry DMSO in a fritted glass tube. The electrodes were placed in a five-neck electrochemical cell together with means for either bubbling or blanketing the solution with gas. Voltammograms were collected using Aftermath software provided by Pine Research. Careful cleaning of the electrodes was performed by polishing with 0.05 µm alumina-particle suspension, Allied High Tech Products, Inc, Rancho Dominguez, CA, USA, on a moistened polishing microcloth to eliminate potential film formation [45].

3.3. RRDE Study

Stock solutions of 0.022 M celastrol in anhydrous DMSO were used in trials. For the experiment, a solution of 0.1 M TBAB in anhydrous DMSO was bubbled for 5 min with a dry O_2/N_2 (35%/65%) gas mixture to establish the dissolved oxygen level in the electrochemical cell. The Au disk electrode was then rotated at 1000 rpm while the disk was swept from 0.2 V to −1.2 Volts and the ring was held constant at 0 Volts; the disk voltage sweep rate was set to 25 mV/s. The molecular oxygen reduction peak ($O_2 + e^- \rightarrow O_2^{-\bullet}$) was observed at the disk electrode at −0.6 volts; the oxidation current ($O_2^{-\bullet} \rightarrow O_2 + e^-$) is observed at the ring electrode. An initial blank was run on this solution, and the ratio of the peak ring current to disk current was calculated as the "collection efficiency" in the absence of antioxidant. Next, an aliquot of the antioxidant was added, the solution bubbled with the gas mixture for 5 min, and the CV rerecorded. Again, the reduction and oxidation peaks were measured and the collection efficiency was calculated. Any decrease in the collection efficiency was due to the amount of superoxide removed by the antioxidant.

3.4. Diffraction Study

The molecular structure of celastrol was determined at low temperature (125 K), and deposited at the CSD database, with Deposition Number 2036458. Crystal Data are reported in Table 1. Single crystal X-ray diffraction data were collected using a Bruker APEX II diffractometer using λ = Cu Kα 1.54178 Å radiation. Data integration scaling was done using Bruker software. Structure solution and refinement was done using SHELX-L [46]. Heavy (non-hydrogen) atoms were refined with their anisotropic displacement parameters. Hydrogen atoms were placed in calculated positions and refined with a riding model on the atoms they were attached to.

3.5. Computational Study

Calculations were performed using software from Biovia (San Diego, CA, USA). Density functional theory (DFT) code DMol^3 was applied to calculate energy, geometry, and frequencies implemented in Materials Studio 7.0 [47]. We employed the double numerical polarized (DNP) basis set that included all the occupied atomic orbitals plus a second set of valence atomic orbitals, and polarized d-valence orbitals [48]; the correlation generalized gradient approximation (GGA) was applied including Becke exchange [49] and Perdew correlation (PBE) [50]. All electrons were treated explicitly, and the real space cutoff of 5 Å was imposed for numerical integration of the Hamiltonian matrix elements. The self-consistent field convergence criterion was set to the root mean square change in the electronic density to be less than 10^{-6} electron/Å^3. The convergence criteria applied during geometry optimization were 2.72×10^{-4} eV for energy and 0.054 eV/Å for force. Calculations include DMSO solvent effect for proper comparison with RRDE results. Docking and molecular dynamic studies were performed with the CDOCKER package in Discovery Studio 2020 version [51]. For molecular dynamics, we used default conditions.

Author Contributions: Conceptualization, M.S.; methodology, F.C.; validation, M.B.; investigation, M.R. and F.C.; data curation, S.B.; writing—original draft preparation, F.C.; writing—review and editing, M.R. and F.C. All authors have read and agreed to the published version of the manuscript.

Funding: This research received no external funding.

Acknowledgments: Sandra Incerpi and Jens Pedersen for comments to this manuscript, Alessio Caruso for improving Scheme 2 and Chris Gahn for support in computer calculations.

Conflicts of Interest: The authors declare no conflict of interest.

References

1. Setty, A.R.; Sigal, L.H. Herbal medications commonly used in the practice of rheumatology: Mechanisms of action, efficacy, and side effects. *Semin. Arthritis Rheum.* **2005**, *34*, 773–784. [CrossRef] [PubMed]
2. Yang, H.; Chen, D.; Cui, Q.C.; Yuan, X.; Dou, Q.P. Celastrol, a Triterpene Extracted from the Chinese 'Thunder of God Vine,' Is a Potent Proteasome Inhibitor and Suppresses Human Prostate Cancer Growth in Nude Mice. *Cancer Res.* **2006**, *66*, 4758–4765. [CrossRef] [PubMed]
3. Kannaiyan, R.; Muthu, K.S.; Gautam, S. Molecular Targets of Celastrol Derived from Thunder of God Vine: Potential Role in the Treatment of Inflammatory Disorders and Cancer. *Cancer Lett.* **2011**, *303*, 9–20. [CrossRef] [PubMed]
4. Sreeramulu, S.; Gande, S.L.; Goebel, M.; Schwalbe, H. Molecular mechanism of inhibition of the human protein complex hsp90–cdc37, a kinome chaperone–cochaperone, by triterpene celastrol. *Angew. Chem. Int. Ed.* **2009**, *48*, 5853–5855. [CrossRef]
5. Hu, W.; Wang, L.; Du, G.; Guan, Q.; Dong, T.; Song, L.; Xia, Y.; Wang, X. Effects of Microbiota on the Treatment of Obesity with the Natural Product Celastrol in Rats. *Diabetes Metab. J.* **2020**, *44*, 747–763. [CrossRef] [PubMed]
6. Sun, H.; Liu, X.; Xiong, Q.; Shikano, S.; Li, M. Chronic inhibition of cardiac Kir2.1 and HERG potassium channels by celastrol with dual effects on both ion conductivity and protein trafficking. *J. Biol. Chem.* **2006**, *281*, 5877–5884. [CrossRef]
7. Bai, J.P.; Shi, Y.L.; Fang, X.; Shi, Q.X. Effects of demethylzeylasteral and celastrol on spermatogenic cell Ca2+ channels and progesterone-induced sperm acrosome reaction. *Eur. J. Pharmacol.* **2003**, *464*, 9–15. [CrossRef]
8. Aqil, F.; Kausar, H.; Agrawal, A.K.; Jeyabalan, J.; Kyakulaga, A.-H.; Munagala, R.; Gupta, R. Exosomal formulation enhances therapeutic response of celastrol against lung cancer. *Exp. Mol. Pathol.* **2016**, *101*, 12–21. [CrossRef]
9. Zhang, X.; Zhang, T.; Zhou, X.; Liu, H.; Sun, H.; Ma, Z.; Wu, B. Enhancement of oral bioavailability of tripterine through lipid nanospheres: Preparation, characterization, and absorption evaluation. *J. Pharm. Sci.* **2014**, *103*, 1711–1719. [CrossRef]
10. Sanna, V.; Chamcheu, J.C.; Pala, N.; Mukhtar, H.; Sechi, M.; Siddiqui, I.A. Nanoencapsulation of natural triterpenoid celastrol for prostate cancer treatment. *Int. J. Nanomed.* **2015**, *10*, 6835–6846. [CrossRef]

11. Wolfram, J.; Suri, K.; Huang, Y.; Molinaro, R.; Borsoi, C.; Scott, B.; Boom, K.; Paolino, D.; Fresta, M.; Wang, J.; et al. Evaluation of anticancer activity of celastrol liposomes in prostate cancer cells. *J. Microencapsul.* **2014**, *31*, 501–507. [CrossRef]
12. Huang, Y.; Zhou, D.; Hang, T.; Wu, Z.; Liu, J.; Xu, Q.; Xie, X.; Zuo, J.; Wang, Z.; Zhou, Y. Preparation, characterization, and assessment of the antiglioma effects of liposomal celastrol. *Anticancer Drugs* **2012**, *23*, 515–524. [CrossRef] [PubMed]
13. Peng, X.; Wang, J.; Song, H.; Cui, D.; Li, L.; Li, J.; Lin, L.; Zhou, J.; Liu, Y. Optimized preparation of celastrol-loaded polymeric nanomicelles using rotatable central composite design and response surface methodology. *J. Biomed. Nanotechnol.* **2012**, *8*, 491–499. [CrossRef] [PubMed]
14. Li, Z.; Wu, X.; Li, J.; Yao, L.; Sun, L.; Shi, Y.; Zhang, W.; Lin, J.; Liang, D.; Li, Y. Antitumor activity of celastrol nanoparticles in a xenograft retinoblastoma tumor model. *Int. J. Nanomed.* **2012**, *7*, 2389–2398. [CrossRef] [PubMed]
15. Niemela, E.; Desai, D.; Nkizinkiko, Y.; Eriksson, J.E.; Rosenholm, J.M. Sugardecorated mesoporous silica nanoparticles as delivery vehicles for the poorly soluble drug celastrol enables targeted induction of apoptosis in cancer cells. *Eur. J. Pharm. Biopharm.* **2015**, *96*, 11–21. [CrossRef]
16. Qi, X.; Qin, J.; Ma, N.; Chou, X.; Wu, Z. Solid self-microemulsifying dispersible tablets of celastrol: Formulation development, characterization and bioavailability evaluation. *Int. J. Pharm.* **2014**, *472*, 40–47. [CrossRef]
17. Lawrence, T. The Nuclear Factor NF-κB Pathway in Inflammation. *Cold Spring Harb. Perspect. Biol.* **2009**, *1*, a001651. [CrossRef]
18. Lee, J.-H.; Koo, T.H.; Yoon, H.-J.; Haeng, S.; Jin, H.Z.; Lee, K.; Hong, Y.-S.; Lee, J.J. Inhibition of NF-κB activation through targeting iκb kinase by celastrol, a quinone methide triterpenoid. *Biochem. Pharmacol.* **2006**, *72*, 1311–1321. [CrossRef]
19. Zhou, Y.; Li, W.; Wang, M.; Xiao, Y.; Zhang, X.; Zhang, H.; Tong, X. Competitive profiling of celastrol targets in human cervical cancer HeLa cells via quantitative chemical proteomics. *Mol. BioSyst.* **2016**, *13*, 83–91. [CrossRef]
20. Salminen, A.; Lehtonen, M.; Paimela, T.; Kaarniranta, K. Celastrol: Molecular targets of Thunder God Vine. *Biochem. Biophys. Res. Commun.* **2010**, *394*, 439–442. [CrossRef]
21. Peng, B.; Xu, L.; Cao, F.; Wei, T.; Yang, C.; Uzan, G.; Zhang, D. HSP90 inhibitor, celastrol, arrests human monocytic leukemia cell U937 at G0/G1 in thiol-containing agents reversible way. *Mol. Cancer* **2010**, *9*, 79. [CrossRef] [PubMed]
22. Seo, H.R.; Seo, W.D.; Pyun, B.-J.; Lee, B.W.; Jin, Y.B.; Park, K.H.; Seo, E.-K.; Lee, Y.-J.; Lee, Y.-S. Radiosensitization by celastrol is mediated by modification of antioxidant thiol molecules. *Chem. Biol. Interact.* **2011**, *193*, 34–42. [CrossRef] [PubMed]
23. Boridy, S.; Le, P.U.; Petrecca, K.; Maysinger, D. Celastrol targets proteostasis and acts synergistically with a heat-shock protein 90 inhibitor to kill human glioblastoma cells. *Cell Death Dis.* **2014**, *5*, e1216. [CrossRef] [PubMed]
24. Lee, J.Y.; Lee, B.H.; Kim, N.D.; Lee, J.Y. Celastrol blocks binding of lipopolysaccharides to a Toll-like receptor4/myeloid differentiation factor2 complex in a thiol-dependent manner. *J. Ethnopharmacol.* **2015**, *172*, 254–260. [CrossRef]
25. Trott, A.; West, J.D.; Klaic, L.; Westerheide, S.D.; Silverman, R.B.; Morimoto, R.I.; Morano, K.A. Activation of heat shock and antioxidant responses by the natural product celastrol: Transcriptional signatures of a thiol-targeted molecule. *Mol. Biol. Cell* **2008**, *19*, 1104–1112. [CrossRef]
26. Bittner, S. When quinones meet amino acids: Chemical, physical and biological consequences. *Amino Acids* **2006**, *30*, 205–224. [CrossRef]
27. Caruso, F.; Rossi, M.; Pedersen, J.Z.; Incerpi, S. Computational studies reveal mechanism by which quinone derivatives can inhibit SARS-CoV-2. Study of embelin and two therapeutic compounds of interest, methyl prednisolone and dexamethasone. *J. Infect. Public Health* **2020**, in press. Available online: https://www.sciencedirect.com/science/article/pii/S1876034120306717 (accessed on 3 December 2020). [CrossRef]
28. Ryu, Y.B.; Park, S.-J.; Kim, Y.M.; Lee, J.-Y.; Seo, W.D.; Chang, J.S.; Park, K.H.; Rho, M.-C.; Lee, W.S. SARS-CoV 3CL^{pro} inhibitory effects of quinone-methide triterpenes from *Tripterygium regelii*. *Bioorg. Med. Chem. Lett.* **2010**, *20*, 1873–1876. [CrossRef]

29. Zhu, J.; Xu, S.; Li, X.; Wang, J.; Jiang, Y.; Hu, W.; Ruan, W. Infectious bronchitis virus inhibits activation of the TLR7 pathway, but not the TLR3 pathway. *Arch. Virol.* **2020**, *165*, 2037–2043. [CrossRef]
30. Khalili, N.; Karimi, A.; Moradi, M.-T.; Shirzad, H. In vitro immunomodulatory activity of celastrol against influenza A virus infection. *Immunopharmacol. Immunotoxicol.* **2018**, *40*, 250–255. [CrossRef]
31. Tseng, C.-K.; Hsu, S.-P.; Lin, C.-K.; Wu, Y.-H.; Lee, J.-C.; Young, K.-C. Celastrol inhibits hepatitis C virus replication by upregulating heme oxygenase-1 via the JNK MAPK/Nrf2 pathway in human hepatoma cells. *Antivir. Res.* **2017**, *146*, 191–200. [CrossRef] [PubMed]
32. Yu, J.-S.; Tseng, C.-K.; Lin, C.-K.; Hsu, Y.-C.; Wu, Y.-H.; Hsieh, C.-L.; Lee, J.-C. Celastrol inhibits dengue virus replication via up-regulating type I interferon and downstream interferon-stimulated responses. *Antivir. Res.* **2017**, *137*, 49–57. [CrossRef] [PubMed]
33. Narayan, V.; Ravindra, K.C.; Chiaro, C.; Cary, D.; Aggarwal, B.B.; Henderson, A.J.; Prabhu, K.S. Celastrol Inhibits Tat-Mediated Human Immunodeficiency virus (HIV) Transcription and Replication. *J. Mol. Biol.* **2011**, *410*, 972–983. [CrossRef] [PubMed]
34. Caruso, F.; Rossi, M.; Kaur, S.; Garcia-Villar, E.; Molasky, N.; Belli, S.; Sitek, J.D.; Gionfra, F.; Pedersen, J.Z.; Incerpi, S. Antioxidant properties of embelin in cell culture. electrochemistry and theoretical mechanism of scavenging. Potential scavenging of superoxide radical through the membrane cell. *Antioxidants* **2020**, *5*, 382. [CrossRef] [PubMed]
35. Caruso, F.; Paumier, S.; Rossi, M. X-ray Crystal Structure of Embelin and its DFT Scavenging of Superoxide Radical. *J. Comput. Chem.* **2018**, *39*, 1143–1148. [CrossRef] [PubMed]
36. Ledford, H. Coronavirus breakthrough: Dexamethasone is first drug shown to save lives. *Nature* **2020**, *582*, 469. [CrossRef]
37. Caruso, F.; Pedersen, J.Z.; Incerpi, S.; Rossi, M. Molecular mechanism for inhibition of the main Covid-19 protease by its inhibitor emodin and corticosteroids is mediated by Cys145. *Molecules*. Submitted.
38. Fadel, R.; Morrison, A.R.; Vahia, A.; Smith, Z.R.; Chaudhry, Z.; Bhargava, P.; Miller, J.; Kenney, R.M.; Alangaden, G.; Ramesh, M.S.; et al. Early short course corticosteroids in hospitalized patients with COVID-19. *Clin. Infect. Dis.* **2020**, *71*, 2114–2120. [CrossRef]
39. Groom, C.R.; Bruno, I.J.; Lightfoot, M.P.; Ward, S.C. The Cambridge Structural Database. *Acta Cryst.* **2016**, *B72*, 171–179. [CrossRef]
40. Zha, J.; Zhang, Q.; Li, M.; Wang, J.R.; Mei, X. Improving Dissolution Properties by Polymers and Surfactants: A Case Study of Celastrol. *J. Pharm. Sci.* **2018**, *107*, 2860–2868. [CrossRef]
41. Belli, S.; Rossi, M.; Molasky, N.; Middleton, L.; Caldwell, C.; Bartow-McKenney, C.; Duong, M.; Chiu, J.; Gibbs, E.; Caldwell, A.; et al. Effective and Novel Application of Hydrodynamic Voltammetry to the Study of Superoxide Radical Scavenging by Natural Phenolic Antioxidants. *Antioxidants* **2019**, *8*, 14. [CrossRef] [PubMed]
42. Rossi, M.; Wen, K.; Caruso, F.; Belli, S. Emodin scavenging of superoxide radical. X-ray crystal structure, hydrodynamic voltammetry and theoretical studies. *Antioxidants* **2020**, *9*, 194. [CrossRef] [PubMed]
43. Jin, Z.; Du, X.; Xu, Y.; Deng, Y.; Liu, M.; Zhao, Y.; Zhang, B.; Li, X.; Zhang, L.; Peng, C.; et al. Structure of Mpro from SARS-CoV-2 and discovery of its inhibitors. *Nature* **2020**, *582*, 289–293. [CrossRef] [PubMed]
44. Habtemariam, S.; Nabavi, S.F.; Berindan-Neagoe, I.; Cismaru, C.A.; Izadi, M.; Sureda, A.; Nabavi, S.M. Should we try the antiinflammatory natural product, celastrol, for COVID-19? *Phytother. Res.* **2020**, *34*, 1189–1190. [CrossRef] [PubMed]
45. Mayrhofer, K.; Strmcnik, D.; Blizanac, B.; Stamenkovic, V.; Arenz, M.; Markovic, N. Measurement of oxygen reduction activities via the rotating disc electrode method: From Pt model surfaces to carbon-supported high surface area catalysts. *Electrochim. Acta* **2008**, *53*, 3181–3188. [CrossRef]
46. Sheldrick, G.M. Crystal structure refinement with SHELXL. *Acta Cryst.* **2015**, *C71*, 3–8. [CrossRef]
47. Delley, B.J. From molecules to solids with the DMol3 approach. *J. Chem. Phys.* **2000**, *113*, 7756–7764. [CrossRef]
48. Perdew, J.P.; Chevary, J.A.; Vosko, S.H.; Jackson, K.A.; Pederson, M.R.; Singh, D.J.; Fiolhais, C. Atoms, molecules, solids, and surfaces: Applications of the generalized gradient approximation for exchange and correlation. *Phys. Rev.* **1992**, *46*, 6671–6687. [CrossRef]
49. Becke, A.D. Density-functional exchange-energy approximation with correct asymptotic behavior. *Phys. Rev. A* **1988**, *38*, 3098–3100. [CrossRef]

50. Perdew, J.P.; Wang, Y. Accurate and simple analytic representation of the electron-gas correlation energy. *Phys. Rev. B* **1992**, *45*, 13244–13249. [CrossRef]
51. Wu, G.; Robertson, D.H.; Brooks, C.L.; Vieth, M.J. Detailed analysis of grid-based molecular docking: A case study of CDOCKER-A CHARMm-based MD docking algorithm. *J. Comput. Chem.* **2003**, *24*, 1549–1562. [CrossRef] [PubMed]

Publisher's Note: MDPI stays neutral with regard to jurisdictional claims in published maps and institutional affiliations.

© 2020 by the authors. Licensee MDPI, Basel, Switzerland. This article is an open access article distributed under the terms and conditions of the Creative Commons Attribution (CC BY) license (http://creativecommons.org/licenses/by/4.0/).